

AN ADAPTIVE AND PARAMETER-FREE SLOPE LIMITER FOR UNSTRUCTURED COMPRESSIBLE FLOW SOLVER

Gang Wang[1,2,*], Zhi-Kan Liu[1,2], Tian-Yu Lin [1,2], Hui-Yue Wang[1,2]

[1] School of Aeronautics, Northwestern Polytechnical University, Xi'an, 710072, China

[2] National Key Laboratory of Aircraft Configuration Design, Xi'an, 710072, China

*Corresponding Author: wanggang@nwpu.edu.cn

Abstract

Conventional slope limiters in unstructured compressible flow solvers exhibit inherent limitations including significant parameter sensitivity and excessive numerical dissipation in smooth flow regions. This study introduces an adaptive, parameter-free slope limiter based on dynamic flow feature detection to mitigate the stability and dissipation issues associated with limiters. The novel limiter is based on the Venkatakrishnan limiter, and it evaluates the smoothness of the local flow field by introducing a new discontinuity detection function. The new discontinuity detector can detect discontinuous structures and even some weak shock waves in complex flow fields. This performance is accomplished by comprehensively considering the pressure and Mach number fluctuations as well as the pressure gradient differences at the cell interfaces. Building on this foundation, the adaptive limiter dynamically adjusts the limiting intensity based on the local discontinuity detection values. Specifically, it strengthens the gradient constraints near shock waves to suppress numerical oscillations while reducing the limiting effects in smooth regions to maintain the solution accuracy. This adaptive mechanism avoids unnecessary numerical dissipation in smooth regions and simultaneously provides stable numerical solutions in discontinuous regions. Several test cases presented in this paper demonstrate that the novel adaptive limiter can considerably enhance computational stability and convergence speed, thereby effectively reducing the calculation errors associated with drag and heat flux.

Keywords: Slope limiter, Compressible flow, Unstructured grid, Discontinuity detection

1. Introduction

In computational fluid dynamics, limiters are essential for stabilizing solutions on unstructured grids by suppressing non-physical oscillations near large gradients, such as shocks [1-3]. The fundamental principle behind limiters is to restrict the reconstructed variables at the grid-cell interfaces. This ensures that the variations in reconstructed variables remain within a reasonable range based on the values of adjacent cells, such as satisfying the maximum principle [4-7]. Represented by those of Barth and Jespersen [8] and Venkatakrishnan [9], these methods constrain the gradient reconstruction values at cell vertices by limiting their extremum range, thereby ensuring that the reconstructed values do not exceed the minimum/maximum range of the adjacent cell solutions. Owing to the single dimensional gradient limitation, excessive dissipation is easily introduced in smooth regions, and it is difficult to adapt to the complex characteristics of multi-dimensional flow fields. Yang et al. [10] and Park and Kim [11,12] further refined the selection of limiter stencils and limiting strategies by considering multi-dimensional flow physics, as represented by both cell centers and vertices surrounding the cell of interest. However, its limiting function still relies on the extremum criterion within a fixed-topology neighborhood, which inevitably leads to excessive dissipation in smooth regions and fails to dynamically distinguish the differential requirements for the limiting strength of different flow characteristics. An effective approach is to activate the limiter only in discontinuous regions. In recent years, Ollivier and Gooch [13] proposed a strategy to deactivate limiters in the subsonic flow regime. By introducing the hyperbolic tangent function into the Venkatakrishnan limiter, this strategy enables the limiter to be activated only within a specific range. Subsequently, Keiichi and Eiji [14] developed a method that automatically adjusts

https://doi.org/10.71945/icas2026_0241

the limiting strength based on the Mach number, which effectively reduces numerical dissipation in smooth subsonic regions. Nevertheless, deactivating limiters within subsonic regions to reduce numerical dissipation fails to yield a satisfactory balance between numerical stability and dissipation for complex flows including shock–shock interactions. If discontinuous regions within the flow field can be accurately identified and limiting is applied exclusively to these areas, the resolution of the numerical method could potentially be significantly enhanced. Previous work has attempted to address this by constructing a discontinuity detector. Oliveira et al. [15] have identified shocks by scrutinizing the truncation error ratios across coarse and fine grids, as well as the local gradient ratios between left and right sides. Ji et al. [16,17] established a discontinuity detector by considering the Mach number and pressure at cell interfaces and validated the detector on compact gas-kinetic scheme. Further validations over a wider range of test cases reveal that the existing methods still exhibit limitations when applied to complex shock interactions.

To address this issue, this work first develops a more effective parameter-free discontinuity detector to accurately capture shock waves and other discontinuous regions in flow fields. Based on this novel discontinuity detection function, an adaptive free-parameter limiter is proposed by modifying the classic Venkatakrishnan limiter. The core principle lies in the dynamic adjustment of limiter parameters according to the values of the discontinuity detection function. This ensures that the limiter remains largely inactive in smooth flow regions while becoming fully activated in discontinuous regions such as shock waves, effectively suppressing numerical oscillations. The method enables the limiter to dynamically adapt its parameters in response to local flow characteristics, thereby satisfying the differential requirements for limiting strength imposed by different flow features.

As mentioned above, the overall structure of this paper is organized as follows. Section 2 describes the finite volume method and spatial reconstruction approach. Section 3 details the proposed discontinuity detection function and adaptive limiter. In Section 4, a series of two-dimensional and three-dimensional numerical cases are performed to validate the effectiveness of the novel limiter, with comprehensive comparisons with existing methods. Section 5 summarizes the main conclusions of this study.

2. Numerical method

2.1 Governing equations

The integral formulation of the three-dimensional Reynolds-averaged Navier-Stokes (RANS) equations in three Cartesian coordinates was considered:

$$\frac{\partial}{\partial t}\iiint_{\Omega}\boldsymbol{Q}dV+\iint_{\partial\Omega}\boldsymbol{F_c}\cdot\boldsymbol{n}dS=\iint_{\partial\Omega}\boldsymbol{F_v}\cdot\boldsymbol{n}dS \tag{1}$$

where $\boldsymbol{Q}=[\rho\ \rho u\ \rho v\ \rho w\ \rho E]^T$ is a vector of conservative variables, ρ is the fluid density, E is the total energy, and $u,v,w$are the velocity components in the Cartesian coordinates (x,y,z), respectively. $\Omega$is the control volume bounded by closed surface $\partial\Omega$, and dS is a surface element. Further details of the aforementioned convective and viscous terms can be found in the reference [18].

The N-S equations that have been spatially discretized on the control volume can be written as follows:

$$\frac{d\boldsymbol{Q}}{dt}=-\frac{1}{V_i}\left[\sum_{f=1}^{N_f}\left(\boldsymbol{F_c}(Q_{i,j})_f-\boldsymbol{F_v}(Q_{i,j})_f\right)\cdot\boldsymbol{n}_f\Delta S_f\right] \tag{2}$$

where $\boldsymbol{n}_f\Delta S_f$ represents the area vector of the common face S_f between cell i and its neighbor cell j, $\boldsymbol{n}_f$ is the outward normal to this face, ΔS_f is the area of this face, and N_f denotes the number of faces of the control volume. Although the exact inviscid flux $\boldsymbol{F}_c(Q_{i,j})$ is nonlinear, it is typically evaluated by upwind numerical flux schemes, such as the Flux Difference Splitting scheme or Flux Vector Splitting scheme, which can be defined as a function of the conservative variables Q at the interface *f*:

$$\boldsymbol{F}_c(Q_{i,j}) = \boldsymbol{F}_c(Q_f^L, Q_f^R, \boldsymbol{n}_f) \tag{3}$$

where superscripts $(\,)^{L,R}$ denote the left and right values of the interface, respectively. The left and right conservative variables at each cell interface were interpolated from cell-centered values. In the cell-centered finite volume method, the cell interface variables Q_f are extrapolated from the cell-centered values $\bar{Q}_i$ using the gradient ∇Q_i :

$$\begin{aligned} Q_f^R &= \bar{Q}_i + \varphi_i \nabla Q_i \cdot \Delta \boldsymbol{r}_{if} \\ Q_f^L &= \bar{Q}_j + \varphi_j \nabla Q_j \cdot \Delta \boldsymbol{r}_{jf} \end{aligned} \tag{4}$$

where φ denotes a slope limiter function employed to suppress oscillations in discontinuity regions.

2.2 The Venkatakrishnan limiter

The fundamental concept of the limiter is to preserve monotonicity during variable reconstruction. To calculate the scalar variable φ_i, the Venkatakrishnan limiter is provided in Eq. (4)

$$\varphi_i = \min_j \begin{cases} \dfrac{1}{\Delta_2}\left[\dfrac{\left(\Delta_{1,\max}^2+\varepsilon^2\right)\Delta_2 + 2\Delta_2^2\Delta_{1,\max}}{\Delta_{1,\max}^2 + 2\Delta_2^2 + 2\Delta_{1,\max}\Delta_2 + \varepsilon^2}\right] & if\,\Delta_2 > 0 \\ \dfrac{1}{\Delta_2}\left[\dfrac{\left(\Delta_{1,\min}^2+\varepsilon^2\right)\Delta_2 + 2\Delta_2^2\Delta_{1,\min}}{\Delta_{1,\min}^2 + 2\Delta_2^2 + 2\Delta_{1,\min}\Delta_2 + \varepsilon^2}\right] & if\,\Delta_2 < 0 \\ 1 & if\,\Delta_2 = 0 \end{cases} \tag{5}$$

$$Q_{\max} = \max\left(Q_i, \max_j Q_j\right)\ \ \Delta_{1,\max} = Q_{\max} - Q_i$$

$$Q_{\min} = \min\left(Q_i, \min_j Q_j\right)\ \ \Delta_{1,\min} = Q_{\min} - Q_i$$

$$\Delta_2 = \nabla Q_i \cdot \boldsymbol{r}_{if}$$

It is important to note that limiter function (5) must be defined with nondimensional quantities. The parameter ε^2 is defined as:

$$\varepsilon^2 = (K\Delta h)^3 \tag{6}$$

where K usually is user-defined constant that influences solution convergence and numerical stability. It has been reported that if K is set to zero, the limiter is active even in the near-constant regions, which ensures solution stability particularly in discontinuous flow regions [9]. A large value of K implies no limiting at all, thereby accelerating convergence rates and reducing numerical dissipation in smooth flow regimes. Therefore, the appropriate selection of the parameter K is critical for achieving a balance between numerical stabilization and dissipation. However, in practical applications, the complexity of flow scenarios makes it challenging to predetermine an optimal value for the parameter K. To address this challenge, the development of an adaptive limiter that dynamically adjusts the parameter K based on local flow field characteristics is essential.

3. Adaptive and Parameter-Free Slope Limiter

The adaptive strategy requires effective discontinuity detection. While the indicator by Zhang et al. [11] enhances robustness in hypersonic flows and detects strong shocks well, its performance is limited for weak shocks in complex fields. This paper introduces an extra function $f\left(\widetilde{\nabla p^L}, \widetilde{\nabla p^R}\right)$, which incorporates the difference in pressure gradients across a cell interface. This addition significantly improves shock wave detectability within complex scenarios. For second-order spatial discretization using the finite volume method, this discontinuous indicator $\alpha_i \in (0,1)$ at cell *i* is defined as

$$\alpha_i = \prod_{f=1}^{N_f} \alpha_{if} \tag{7}$$

where α_{if} is the discontinuous indicator obtained by the midpoint at the interface *f* around cell *i*, which can be defined by

$$\alpha_{if} = \frac{f\left(\widetilde{\nabla p^L}, \widetilde{\nabla p^R}\right)}{1 + D_{ij}^2}$$

$$D_{ij} = \frac{|p^L - p^R|}{p^L} + \frac{|p^L - p^R|}{p^R} + (Ma_n^L - Ma_n^R)^2 + (Ma_t^L - Ma_t^R)^2$$

$$f\left(\widetilde{\nabla p^L}, \widetilde{\nabla p^R}\right) = \frac{2}{\pi} arctan\left(\left(\left\|\widetilde{\nabla p^L}\right\| + \left\|\widetilde{\nabla p^R}\right\|\right)\left(1 - \left|\frac{\left\|\widetilde{\nabla p^L}\right\| - \left\|\widetilde{\nabla p^R}\right\|}{\left\|\widetilde{\nabla p^L}\right\| + \left\|\widetilde{\nabla p^R}\right\| + \epsilon}\right|\right)\right) \tag{8}$$

$$\epsilon = 10^{-6}$$

$$\widetilde{\nabla p^\iota} = \frac{h_i \nabla p_i}{p_i}, h_i = \Omega_i$$

where p^L and p^R represent the left and right values of the pressure across the midpoint at the interface f around cell i, respectively. Ma_n and Ma_t are the Mach numbers defined by normal and tangential velocity at the face. This combination of parameters allows the detector to effectively distinguish between strong shock discontinuities, which require strong limiting, and regions of high shear or turbulent activity, where limiting should be minimized to preserve the integrity of the flow structures. The inclusion of pressure gradient differences is particularly crucial for accurately capturing shear layers without excessive numerical dissipation. It is evident from Eq. (8) that the value of α_{if} lies between 0 and 1, where 1 is considered smooth and 0 is considered non-smooth. And when there is a significant difference between the left and right values of the interface f around cell i, the value of α_{if} approaches zero. The characteristic length h_i used for local nondimensionalize of p^L is derived from the volume of the cell adjacent to the interface. The term ϵ within function $f\left(\widetilde{\nabla p^L}, \widetilde{\nabla p^R}\right)$ acts as a safeguard against division by zero. Additionally, it is important to note that when there is a significant difference in pressure gradients that are also closely matched, $\left\|\widetilde{\nabla p^L}\right\| - \left\|\widetilde{\nabla p^R}\right\|$ tends toward zero, which necessitates the inclusion of the absolute value of the pressure gradient. Consequently, $1 - \left|\frac{\left\|\widetilde{\nabla p^L}\right\| - \left\|\widetilde{\nabla p^R}\right\|}{\left\|\widetilde{\nabla p^L}\right\| + \left\|\widetilde{\nabla p^R}\right\| + \epsilon}\right|$ is multiplied by $\left\|\widetilde{\nabla p^L}\right\| + \left\|\widetilde{\nabla p^R}\right\|$.

The core idea behind the newly proposed adaptive limiter is to modulate the parameter K so that it tends towards infinity in the smooth flow regions and decreases in the regions with strong discontinuities. This study utilizes Eq. (9) to adaptively modulate the limiting region of the limiter within the flow field.

$$\varepsilon^2 = \left[tan\left(\frac{\pi}{2}\alpha_i\right)\Delta h\right]^3 \tag{9}$$

where α_i is the discontinuous indicator in Eq. (7). This paper refers to this limiter as Venkatakrishnan-adpt. In regions of flow discontinuities, the discontinuous indicator approaches zero, and the limiter fully activates to suppress numerical oscillations. In smooth flow regions, the discontinuous indicator approaches unity, while the parameter ε^2 tending towards infinity. The present modification is simple and it does not require any manually specified parameters. The impact of this newly proposed adaptive limiter on the convergence characteristics of the flow field and the solution accuracy will be discussed in detail in the following section.

4. Results and Discussion

The methods described above have been implemented into an in-house flow solver (HUNS3D-HPC)[19-22] based on hybrid unstructured mesh. In this section, numerical test cases are introduced to verify the accuracy, robustness, and efficiency of the newly proposed adaptive limiter and other limiters, such as the Venkatakrishnan and Barth-Jespersen limiters, are also tested for comparison.

4.1 Ringleb's flow

The flow solution proposed by Ringleb represents an analytical solution to the steady nonlinear Euler equations for a flow bounded by a wall. For most of the related literature [23-25], the Ringleb flow was selected because it represents a transonic flow, and an exact solution is available for comparison. In this study, we used the analytic solution of the Ringleb flow to test the accuracy of different limiters. The Ringleb flow was solved using hodograph plane transformation. Thus, the physical location *(x, y)* is given in terms of the physical variables (V,θ), and a solution can be obtained:

$$\psi = \frac{\sin\theta}{V} \quad k = \frac{1}{\psi}$$
$$x(\psi,V) = \frac{1}{\rho}\left[\frac{1}{2V^2} - \psi^2\right] + \frac{L}{2} \quad y(\psi,V) = \pm\frac{\psi}{\rho V}\sqrt{1 - V^2\psi^2} \tag{10}$$

where ψ is the stream function, V is the velocity magnitude, and θ is the flow angle measured from the x axis., and ρ and L are functions of V.

$$\rho = b^5 \quad L = \frac{1}{b} + \frac{1}{3b^3} + \frac{1}{5b^5} - \frac{1}{2}\ln\left(\frac{1+b}{1-b}\right)$$
$$b = \sqrt{1 - 0.2V^2} \quad p = b^7 \tag{11}$$

Fig. 1 shows the computational domain along the solid walls at the streamlines for $k_{\min} = 0.55$ $k_{\max} = 1.2$ and placing the inlet and outlet at V = 0.5. As shown in Fig. 2, the subsonic flow (with a Mach number of approximately 0.5) entered from the top boundary, traversed the computational domain, and exited the bottom boundary with a maximum Mach number of 1.35.

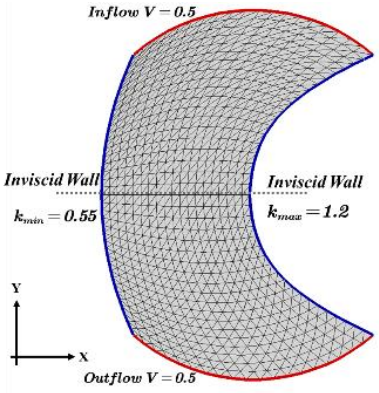


Figure. 1 Computational mesh of Ringleb's flow

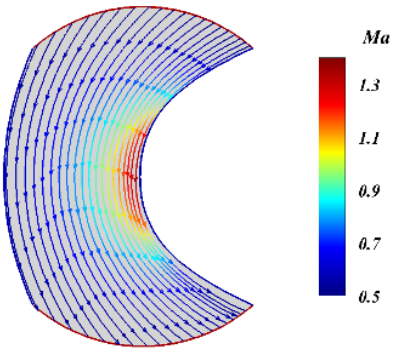


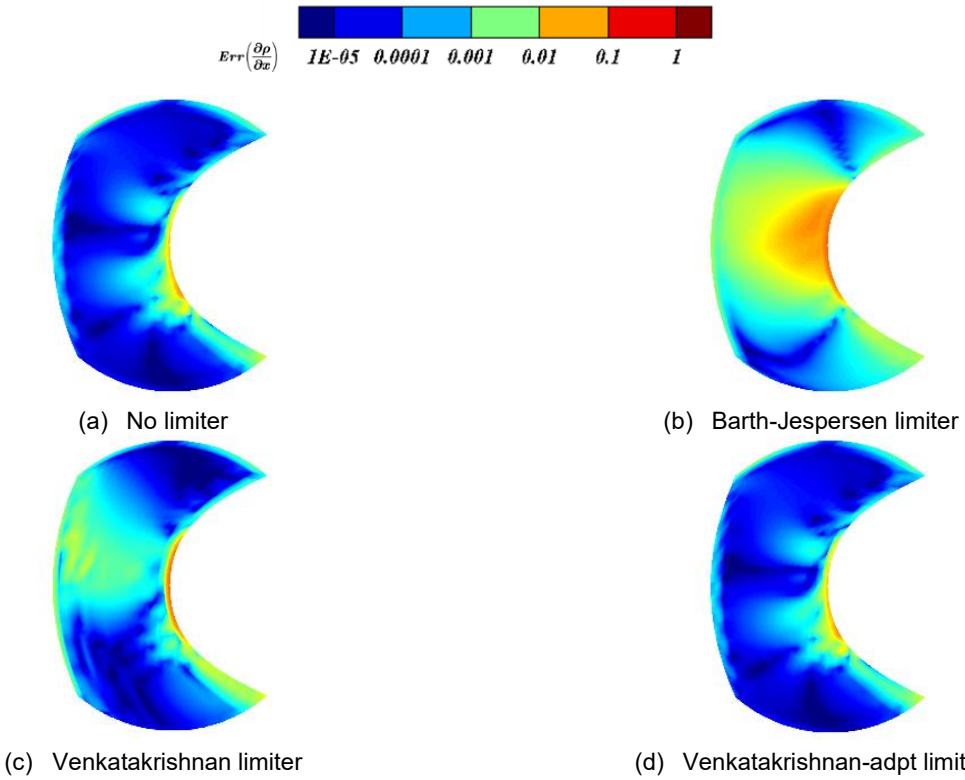
Figure. 2 Flow field features

Fig. 3 depicts the error distribution for the density derivative in both the x-directions, as derived from numerical solutions utilizing various limiters. Given that the analytical value of density at any given point can be computed using Eq. (12), we employ the formula to accurately determine the density derivatives in both the x direction:

$$\frac{\partial\rho}{\partial x} = \frac{\rho(x+\varepsilon,y) - \rho(x,y)}{\varepsilon} \quad \varepsilon = 1e^{-6} \tag{12}$$

Given the absence of shock waves in Ringleb flow, the flow field derived without employing any limiters is expected to be optimal. Fig. 3 (a) demonstrates that the solution without the limiter exhibits the least error, whereas the incorporation of limiters tends to amplify the error of the solution. Compared to the Barth-Jespersen and Venkatakrishnan limiters (K=1.0), the adaptive Venkatakrishnan limiter significantly enhances the accuracy of gradient solutions, particularly in regions close to the inner wall. It is evident that the activation of the limiter in these regions introduces additional errors in the gradient solutions; however, the adaptive Venkatakrishnan limiter effectively preserves the accuracy of the

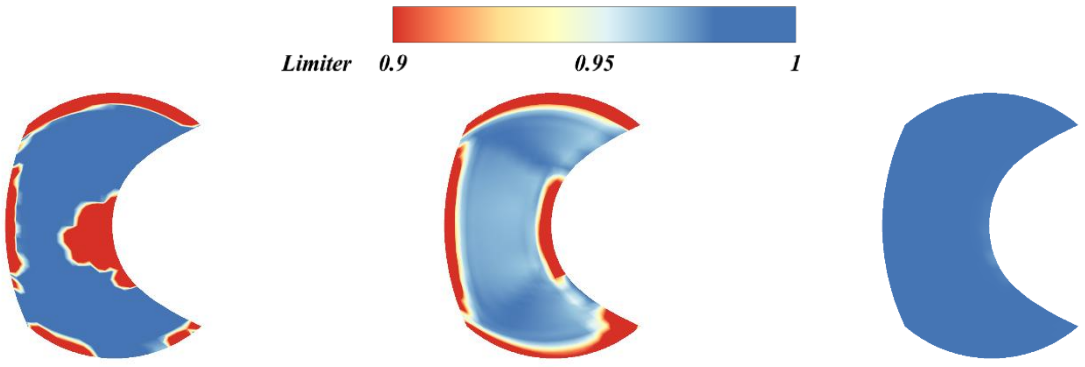
gradient solutions in smooth flow areas. We analyzed the limiter function values associated with density gradients following the implementation of these two limiters. Fig. 4 shows the contour of the limiter value for the density gradient magnitude. The numerical results demonstrate that the conventional Barth-Jespersen and Venkatakrishnan limiters exhibit significant limiting effects in boundary regions (particularly near the walls), whereas the adaptive limiter maintains an ideally inactive state throughout the entire computational domain. These results verify that, in flow fields without physical discontinuities, the adaptive limiter can accurately identify and avoid unnecessary numerical limiting, demonstrating superior performance to traditional methods.



(a) No limiter (b) Barth-Jespersen limiter

(c) Venkatakrishnan limiter (d) Venkatakrishnan-adpt limiter

Figure. 3 The error distribution of the density derivative along the x direction



(a) Barth-Jespersen limiter (b) Venkatakrishnan limiter (c) Venkatakrishnan-adpt limiter

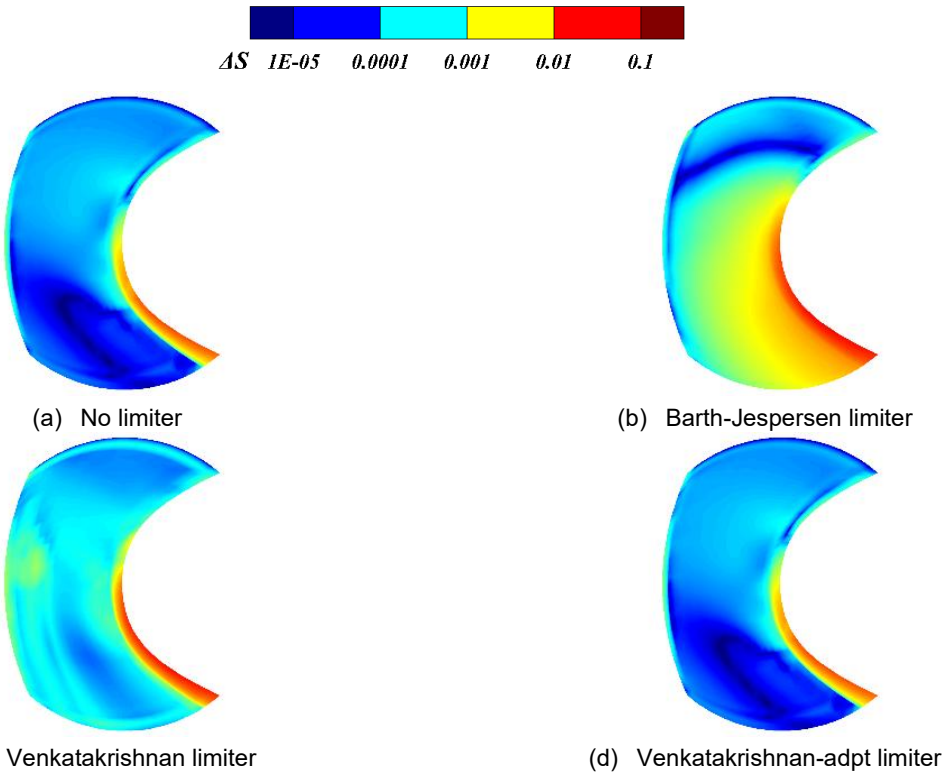
Figure. 4 Limiter value for density gradient

For the Ringleb flow, owing to the absence of viscosity and shock waves, the analytical value of entropy production in the flow field should be zero. This study provides a definition of entropy production relative to inflow as follows:

$$\Delta S = \frac{p/p_{in}}{(\rho/\rho_{in})^{\gamma}} - 1 \tag{10}$$

Fig. 5 illustrates the variation in entropy production derived from the numerical solutions employing various limiters. The Barth-Jespersen and Venkatakrishnan limiters yield significantly higher entropy production in proximity to the inner wall, as opposed to the adaptive limiter. This is primarily attributed

to the fact that the unreasonable activation of the limiter near the inner wall in Fig. 5(b) and 5(c) leads to a decrease in accuracy and an increase in numerical dissipation.



(a) No limiter (b) Barth-Jespersen limiter

(c) Venkatakrishnan limiter (d) Venkatakrishnan-adpt limiter

Figure. 5 Entropy production from the freestream value for Ringleb's flow

4.2 Opposing Jet

In this section, we analyze a supersonic flow scenario where a freestream Mach number of 3.98 envelops a hemispherical nose, which is perturbed by an opposing sonic jet aligned along its axis. As depicted in Figure. 6, the model configuration consists of a hemispherical blunt body with a diameter of d_m. The sonic nozzle has a diameter of d_j. The flow field, modified by the opposing jet, is illustrated in Figure. 7. Based on previous experimental data [26,27], we assume an ideal gas for both the freestream and the jet. The freestream's total pressure $P_{0,\infty}$ = 1370 kPa, total temperature $T_{0,\infty}$ = 397 K, and Ma_∞ = 3.98, while the corresponding parameters for the opposing jet are $P_{0,j}$ = 1096 kPa, $T_{0,j}$ = 295 K, Ma_j = 1.0, respectively. Fig. 8 presents the computational grid distribution utilized in this study. The numerical analysis model was deliberately constructed to match that of Hayashi for comparative purposes.

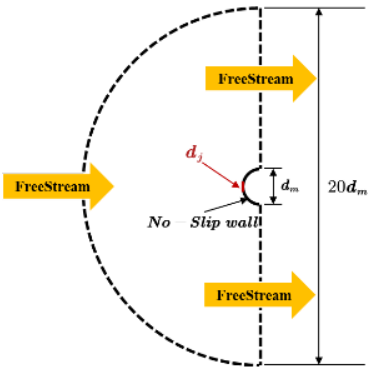


Figure. 6 Source area for computation domain

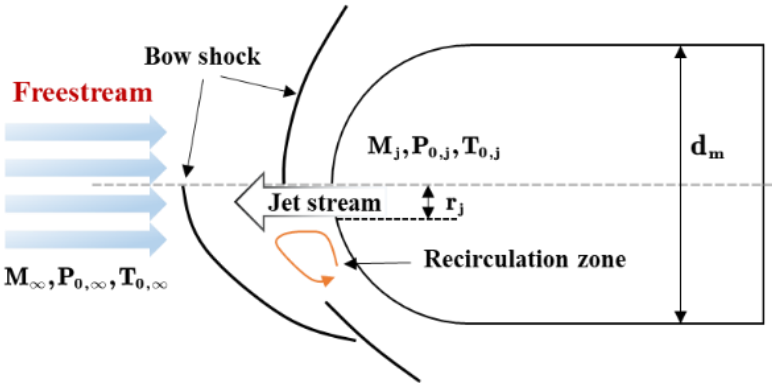


Figure. 7 Principal features of opposing jet

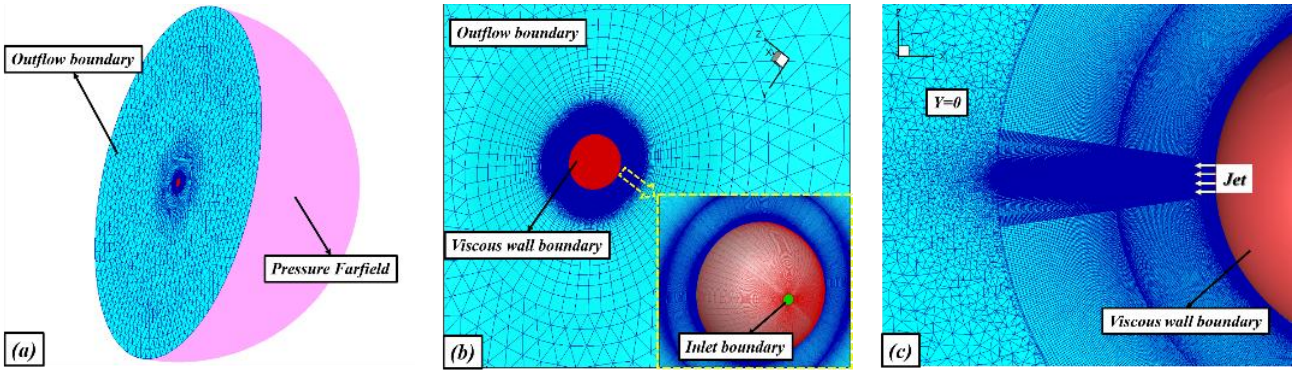


Figure. 8 Computational domain and boundary conditions of the opposing jet

As shown in Fig. 9, the improved surface heat flux distribution prediction links directly to more accurate resolution of near-wall flow structures and thermal boundary layer, which are governed by shear and turbulent transport. The adaptive limiter's lower dissipation in smooth regions enables more physical wall-bounded flow development, leading to better agreement with experimental data. This proves the proposed adaptive limiter benefits heat flux computation convergence acceleration. Compared with Hayashi et al. experimental and numerical data, the adaptive computation's heat flux results align better with experiments than reference numerical solutions, especially in capturing peak heat flux magnitude and location.

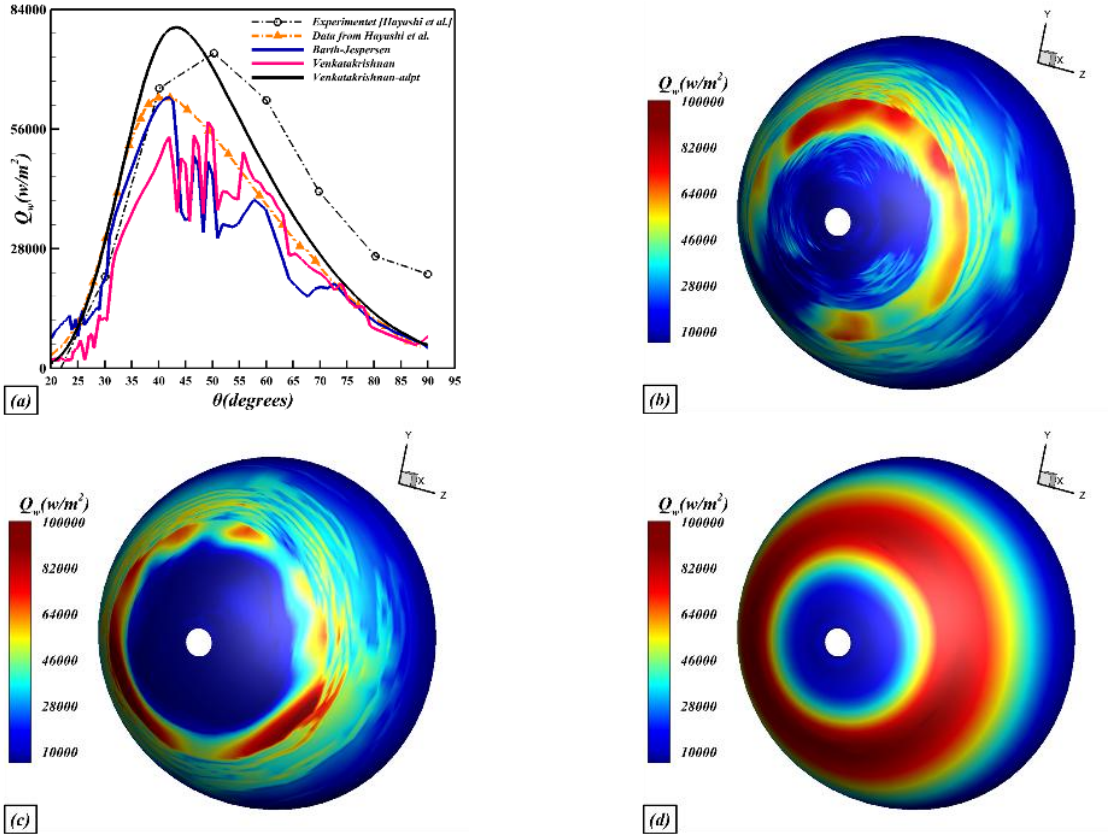
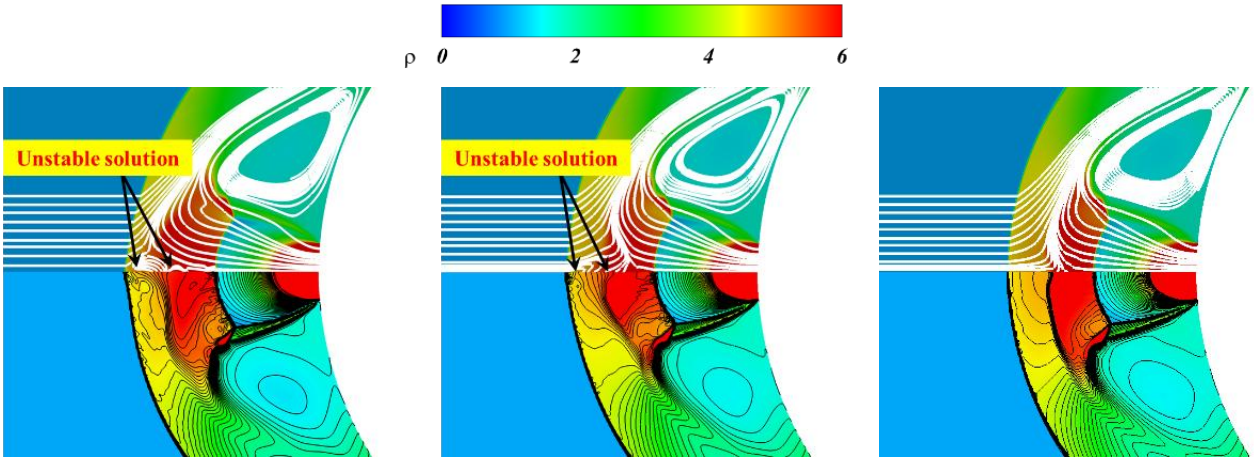


Figure. 9 Heat flux distributions (a) along the cross-section Y=0, (b) Barth-Jespersen limiter, (c) Venkatakrishnan limiter ,(d) Venkatakrishnan-adpt limiter

Fig. 10 compares the density contours obtained using different limiters. Simulations utilizing the Barth-Jespersen and Venkatakrishnan limiters exhibit significant numerical oscillations within the shear layer formed between the freestream and the opposing jet, as well as around the recirculation zone downstream of the jet orifice. These oscillations artificially thicken the shear layer and distort the vortical structures. In contrast, the flow field simulated with the proposed adaptive limiter shows a markedly cleaner and crisper resolution of these fine-scale flow features. The shear layer interface is sharper, and the stagnation region is more stable, demonstrating the limiter's ability to adapt to both strong discontinuities and regions of high shear, which is paramount for accurate simulation of turbulence and shear flow phenomena.



(a) Barth-Jespersen limiter (b) Venkatakrishnan limiter (c) Venkatakrishnan-adpt limiter

Figure. 10 Density contours of the opposing jet

4.3 Reusable launch vehicles

In this section, the opposing jet during rocket recovery is analyzed to verify the application potential of the adaptive limiter in complex flows. The intense interaction between the high-speed freestream and the jet involved in this flow gives rise to a complex structure comprising a bow shock, jet boundary layer, shear layer, and recirculation zone. This flow structure is accompanied by flow instabilities such as multi-shock interference and unsteady oscillations, which impose high requirements on the robustness and resolution of numerical methods.

The physical model used in this study from the RETALT (Retro Propulsion Assisted Landing Technologies) project under the framework of the European Union's "Horizon 2020" program, specifically the typical RETALT1 configuration therein. Fig. 11 shows the geometric configuration and computational mesh distribution of this configuration; detailed geometric parameters, boundary condition settings, and operating condition designs can be found in References [28-30]. Table 1 summarizes the key parameters of the freestream conditions and nozzle jet.

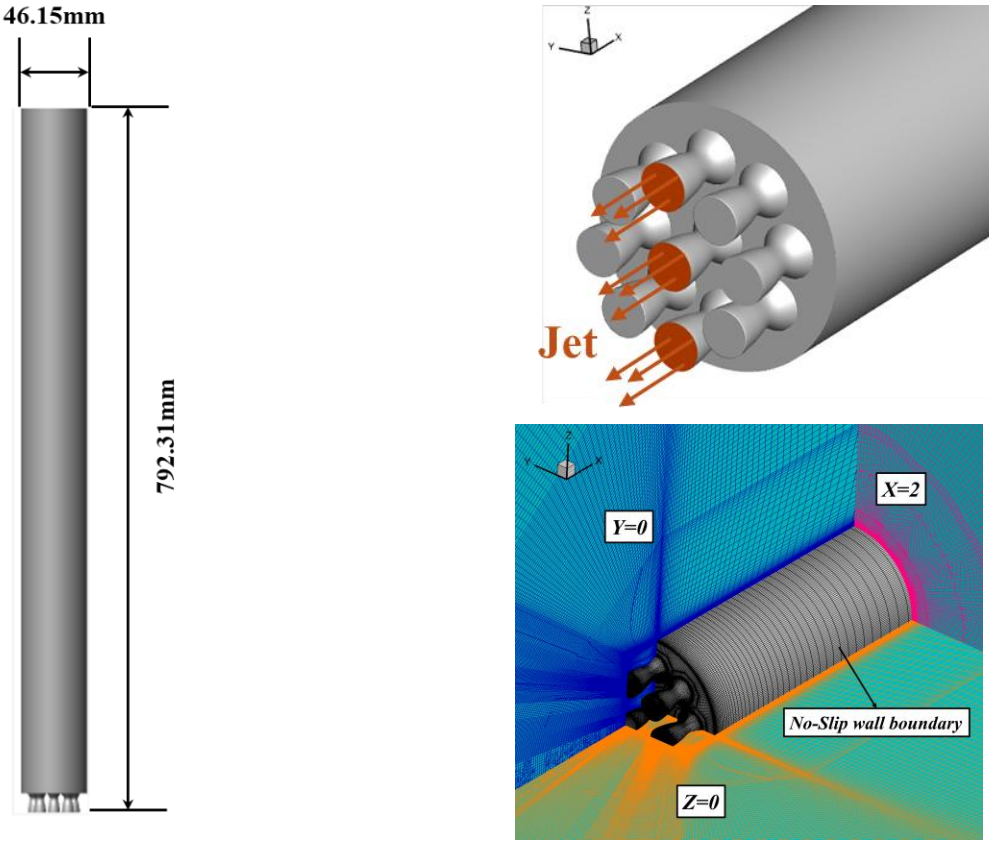


Figure. 11 RETALT1 configuration and different cross-sectional mesh distributions

Table 1 Hypersonic retro propulsion for reusable launch vehicles

	Parameter	Value
Freestream	Mach number	5.29
	Stagnation pressure[kPa]	400
	Stagnation temperature[K]	450
Nozzle exit	Mach number	2.44
	Thrust coefficient (Ct)	4.0
	Stagnation temperature[K]	300
	Wall temperature[K]	200

Fig. 12 compares the convergence histories of drag coefficients for different limiters within 20,000 iterations. It can be observed that the adaptive Venkatakrishnan limiter has almost converged in drag coefficient at approximately 10,000 iterations. In contrast, the computational results of the standard Venkatakrishnan limiter (K = 1.0) and the Barth-Jespersen limiter still exhibit persistent oscillations even after 20,000 iterations. This result indicates that, when simulating such complex flows, introducing the adaptive mechanism can effectively enhance the convergence speed and stability of numerical computations

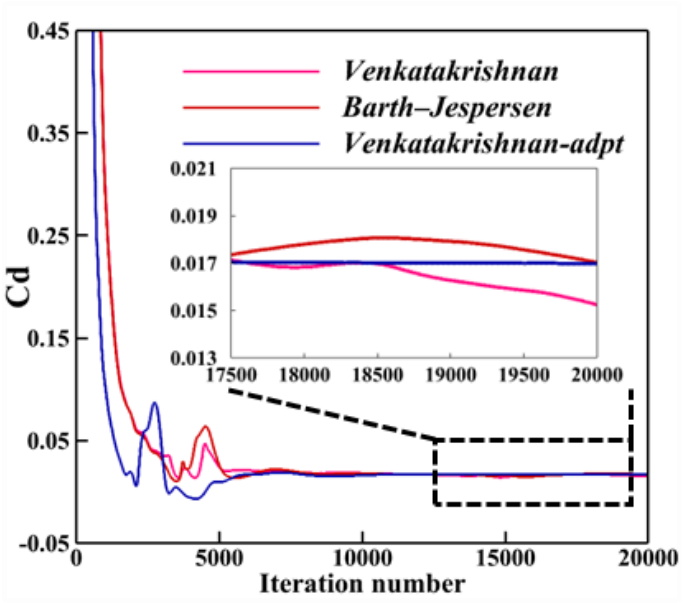
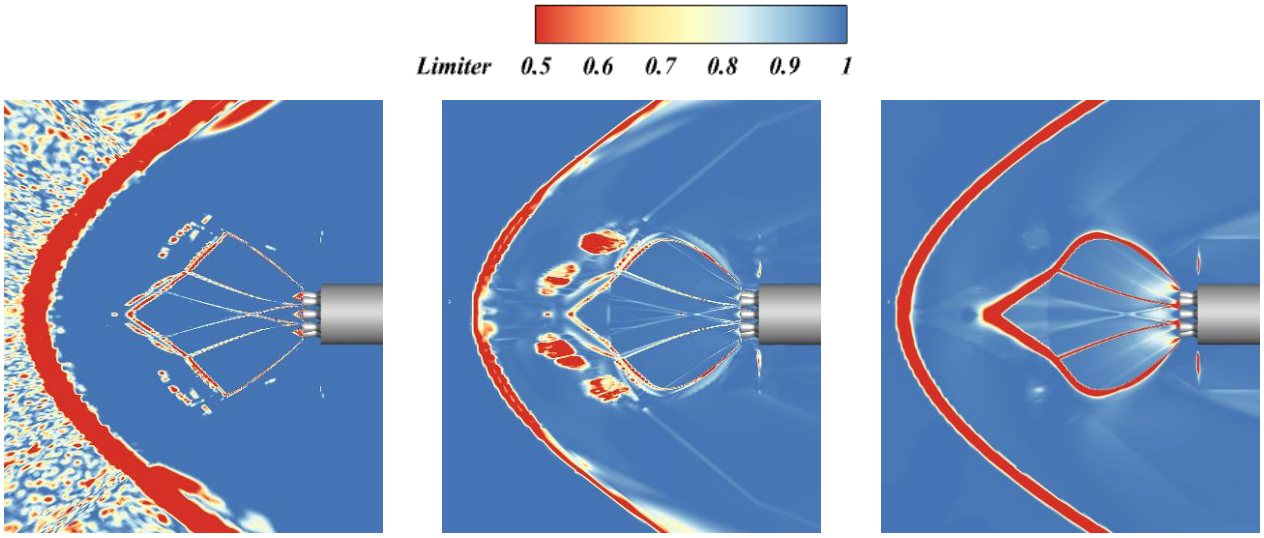


Figure. 12 Drag coefficient convergence history

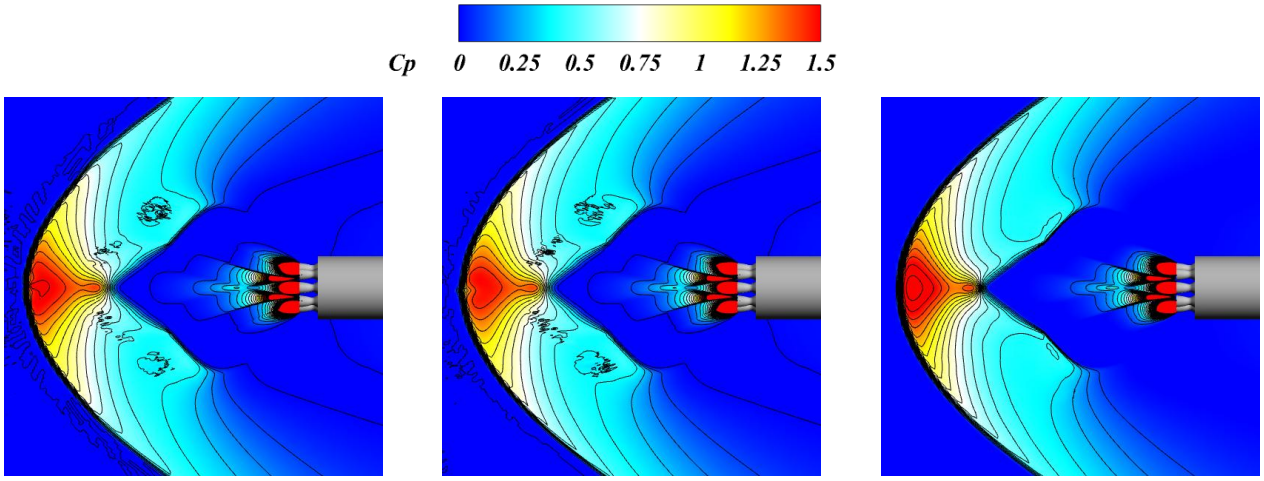
Fig. 13 illustrates the behavioral differences of the three limiters in complex wave structures through the distribution of limiter values corresponding to density gradients. In this three-nozzle jet interaction case, the interaction between jets gives rise to a complex shock system downstream, comprising multiple oblique shocks and reflected shocks, while the freestream, obstructed by the jets, forms a bow shock. As observed from the limiter distribution, all three limiters exhibit small values in shock regions, effectively exerting their limiting effect and thus enhancing the resolution of shock capturing. However, the Barth-Jespersen limiter also imposes considerable limiting in smooth regions such as the freestream region and downstream of the jet oblique shock, which is clearly inconsistent with physical expectations. The Venkatakrishnan limiter still introduces unnecessary numerical dissipation in the region downstream of the jet oblique shock. In contrast, the adaptive limiter adopted in this study is activated only in key regions such as the bow shock and jet shocks, while its value is close to 1.0 in other flow regions, effectively avoiding unnecessary interference with smooth flow regions.



(a) Barth-Jespersen limiter (b) Venkatakrishnan limiter (c) Venkatakrishnan-adpt limiter

Figure. 13 Limiter value for density gradient

Fig. 14 presents the contour of the pressure coefficient. It can be observed that the numerical simulations employing the Barth-Jespersen limiter and the Venkatakrishnan limiter exhibit oscillations downstream of the jet oblique shock. This phenomenon may be associated with the unreasonable limiting behavior at this location analyzed in Fig. 13, leading to non-convergence of numerical results in this region. Meanwhile, the flow field at the bow shock obtained by these two limiters also shows slight oscillations. In contrast, the flow field derived from simulations with the adaptive limiter displays a relatively smoother results both near the detached shock and downstream of the jet oblique shock. This observation suggests that the implementation of an adaptive limiter is adopted at moderating gradients in discontinuities, thereby yielding a clearer and more stable shock structure.



(a) Barth-Jespersen limiter (b) Venkatakrishnan limiter (c) Venkatakrishnan-adpt limiter

Figure. 14 Pressure contours of the opposing jet

5. Conclusion

This paper presents an implementation method for a widely applicable parameter-free adaptive slope limiter designed for unstructured grids. The adaptive limiter incorporates a novel discontinuity detection function capable of accurately identifying complex shock structures and weak discontinuities, activating only in the vicinity of the discontinuities. It ensures high-resolution solutions in smooth flow regions, while effectively suppressing numerical oscillations in discontinuous areas, thereby achieving high-resolution numerical solutions. Numerical results demonstrate that the limiter, based on this adaptive strategy, retains the convergence advantages of the Venkatakrishnan limiter while significantly improving the convergence rate and accuracy of the wall drag and heat flux calculations. Since only minor modifications are required to the reconstruction procedure, the novel limiter can be readily incorporated into existing solvers with negligible extra computational cost. More importantly, the limiter

eliminates the need for manual parameters and exhibits excellent robustness and reproducibility, thereby providing an efficient and reliable solution for high-resolution numerical simulations of complex flow fields.

6. Acknowledgements

The research was supported by the National Natural Science Foundation of China (No.U23B6009, and No.U2570218). The computations were conducted in Computing Center in Xi'an. The authors thankfully acknowledge these institutions.

7. Copyright Statement

The authors confirm that they, and/or their company or organization, hold copyright on all of the original material included in this paper. The authors also confirm that they have obtained permission, from the copyright holder of any third party material included in this paper, to publish it as part of their paper. The authors confirm that they give permission, or have obtained permission from the copyright holder of this paper, for the publication and distribution of this paper as part of the ICAS proceedings or as individual off-prints from the proceedings.

References

[1] Tang, Shujiang, and Mingjun Li. Construction and application of several new symmetrical flux limiters for hyperbolic conservation law. Computers & Fluids, Vol. 213 , 2020, pp.1-13.

[2] Schwarz, Anna, Jens Keim, Simone Chiocchetti, Andrea Beck. A reinforcement learning based slope limiter for second-order finite volume schemes. Proceedings in applied mathematics and mechanics, Vol. 23, No. 1,2023, 202200207.

[3] Valle N, Álvarez-Farré X, Gorobets A, et al. On the implementation of flux limiters in algebraic frameworks. Computer Physics Communications, Vol. 271, 2022, pp. 108230.

[4] Nishikawa, Hiroaki. Updates to implicit edge-based gradient methods. AIAA SciTech 2024 Forum, AIAA Paper 2024: 1748.

[5] K. Kitamura, T. Aogaki, A. Inatomi, et al. Postlimiters and Simple Dirty-Cell Detection for Three-Dimensional Unstructured (Unlimited) Aerodynamic Simulations. AIAA Journal, Vol.56, No. 8, 2018, pp.3192-3204.

[6] Kitamura K, Kitamura K. Reconstruction and Slope Limiters. Advancement of Shock Capturing Computational Fluid Dynamics Methods: Numerical Flux Functions in Finite Volume Method, 2020, pp. 117-136.

[7] Zhou, Tong, and Haitao Dong. A fourth-order entropy condition scheme for systems of hyperbolic conservation laws. Engineering Applications of Computational Fluid Mechanics, Vol. 15, No.1, 2021, pp.1259-1281.

[8] Barth, Timothy, and Dennis Jespersen. The design and application of upwind schemes on unstructured meshes. 27th Aerospace sciences meeting, AIAA Paper, 1989: 366.

[9] Venkatakrishnan, Venkat. Convergence to steady state solutions of the Euler equations on unstructured grids with limiters. Journal of computational physics, Vol. 118, 1995, pp. 120–130.

[10] Yang, Minghao, and Shu Li. An efficient implementation of compact third-order implicit reconstruction solver with a simple WBAP limiter for compressible flows on unstructured meshes. Engineering Applications of Computational Fluid Mechanics , Vol. 17, No. 1, 2023: 2249135.

[11] Park J S, Kim C. Multi-dimensional limiting process for finite volume methods on unstructured grids. Computers & Fluids, Vol. 65, 2012, pp. 8-24.

[12] Park, Jin Seok, Sung-Hwan Yoon, and Chongam Kim. Multi-dimensional limiting process for hyperbolic conservation laws on unstructured grids. Journal of Computational Physics, Vol. 229, No. 3, 2010, pp.788-812.

[13] Kitamura K, Shima E. Simple and parameter-free second slope limiter for unstructured grid aerodynamic simulations. AIAA Journal, Vol. 50, No. 6, 2012, pp.1415-1426.

[14] Michalak C, Ollivier-Gooch C. Accuracy preserving limiter for the high-order accurate solution of the Euler equations. Journal of Computational Physics, Vol. 228, No. 23, 2009, pp. 8693-8711.

[15]Liu C, Oliveira M. New shock detector for shock-boundary layer interaction[C]//High Performance Computing and Applications: Second International Conference, HPCA 2009, Shanghai, China, August 10-12, 2009, Revised Selected Papers. Springer Berlin Heidelberg, 2010: 78-87.

[16] Ji Xing, Shyy Wei, Xu Kun. A gradient compression-based compact high-order gas-kinetic scheme on 3D hybrid unstructured meshes. International Journal of Computational Fluid Dynamics, Vol. 35, No. 7, 2021, pp.485-509.

[17]Zhang Yue, Ji Xing, Xu Kun. A High-Order Compact Gas-Kinetic Scheme in a Rotating Coordinates Frame and on Sliding Mesh. International Journal of Computational Fluid Dynamics, Vol. 37, No. 3, 2023, pp. 181-200.

[18]Wang, Gang, and Z. Y. Ye. Mixed element type unstructured grid generation and its application to viscous flow simulation. 24th International congress of aeronautical sciences. 2004.

[19]Wang G, Li Q, Liu Y. “IDDES method based on differential Reynolds-stress model and its application in bluff body turbulent flows,” Aerospace Science and Technology, Vol. 119, 2021, 107207.

[20]Zhou H, Wang G, Mian H H, et al. Fluid-structure coupled analysis of tandem 2D elastic panels. Aerospace Science and Technology, Vol. 111, 2021, 106521.

[21]Wang G, Zhou H. Investigation of Multiple-Equilibrium-Points Phenomena in Transonic Flutter of NACA 64A010 Airfoil. AIAA Journal, Vol. 60, No. 9, 2022, pp. 5581-5588.

[22]Wang G, Li Q, Sun X. Resolution assessment of Reynolds stress model-based DES methods for high-lift device flow over 30P30N configuration. Aerospace Science and Technology, Vol. 145, 2024, 108863.

[23]Satav V, Hixon R, Nallasamy M. Validation of a computational aeroacoustics code for nonlinear flow about complex geometries using Ringleb's flow. 11th AIAA/CEAS Aeroacoustics Conference. AIAA Paper, 2005: 2871.

[24]Meng X, Gu Y, Hu G. A fourth-order unstructured NURBS-enhanced finite volume WENO scheme for steady Euler equations in curved geometries. Communications on Applied Mathematics and Computation, Vol. 5, No. 1, 2023, pp. 315-342.

[25]Giuliani A. A two-dimensional stabilized discontinuous Galerkin method on curvilinear embedded boundary grids. SIAM Journal on Scientific Computing, Vol. 44, No. 1, 2022, pp. A389-A415.

[26]Hayashi K, Aso S, Tani Y. Numerical study on aerodynamic heating reduction by opposing jet. Memoirs of the Faculty of Engineering, Kyushu University, Vol.61, 2006, pp.39-54.

[27]Hayashi K, Aso S, Tani Y. Numerical study of thermal protection system by opposing jet. 43rd AIAA Aerospace Sciences Meeting and Exhibit, AIAA Paper, 2005: 188.

[28]Gülhan A, Marwege A, Vos J. Retro propulsion assisted landing technologies: the RETALT project. CEAS Space Journal, Vol. 14, No.3, 2022, pp. 431-432.

[29]Marwege A, Gülhan A, Klevanski J, et al. RETALT: review of technologies and overview of design changes. CEAS Space Journal, Vol. 14, No.3, 2022, pp. 433-445.

[30]Marwege A, Kirchheck D, Klevanski J, et al. Hypersonic retro propulsion for reusable launch vehicles tested in the H2K wind tunnel. CEAS Space Journal, Vol. 14, No.3, 2022, pp. 473-499.